nature communications

Article

https://doi.org/10.1038/s41467-026-68951-x

Ultralow CNT-reinforced phase-change fibers for scalable wearable thermoregulation

Received: 14 July 2025

Accepted: 21 January 2026

Published online: 31 January 2026

Check for updates

Xiaoye Geng[1], Ziyu Wang[1], Feng Xiong[1], Lifang Liu[2], Ziting Zhen[1], Yongkang Jin[1], Mulin Qin[1], Jianwen Su[3], Song Gao[1], Yonggang Wang[1], Qining Wang[4] ✉ & Ruqiang Zou[1,5] ✉

Phase-change materials (PCMs) demonstrate transformative potential for wearable thermal management systems; however, their practical implementation faces challenges due to trade-offs among energy storage density, mechanical robustness, and phase-change stability. Here, we present a nanotechnology-directed strategy that integrates ultralow carbon nanotubes (CNT, 0.1 wt.%) scaffolds with three-dimensional (3D) interpenetrating polymer networks (IPNs), achieving remarkable synergy between crystallinity control and thermal regulation. The resultant phase-change fibers (PCFs) demonstrate dual-functional optimization. Firstly, they exhibit excellent latent heat storage (ΔH_m = 139.0 J·g^{-1}, ΔH_c = 138.0 J·g^{-1}) with remarkable thermal stability, enabled by CNT-induced heterogeneous nucleation. Secondly, the PCFs show high mechanical robustness (ε = 1530%, σ = 6.32 MPa) and photothermal energy harvesting efficiency (η = 90.5%, at 120 mW·cm^{-2}). These enhancements are attributed to CNT network-enhanced interfacial thermal coupling. Furthermore, the fibrous architectures enable high-fidelity (>98%) cutting/sewing during textile manufacturing, facilitating scalable production of energy-efficient thermal-regulating fabrics. This establishes a universal framework for scalable smart textiles and bridges the gap between laboratory-level phase-change engineering and industrial-scale wearable thermal systems. This strategy advances the development of self-regulating textiles with on-demand thermal responsiveness, paving the way for next-generation smart fabrics for energy-efficient personal thermal management.

Global thermal management systems are at a critical inflection point: the building sector consumes 40% of global energy and contribute 36% of anthropogenic CO_2 emmiissions[1]. Conventional heating, ventilation, and air conditioning (HVAC) systems are highly inefficient, achieving thermal efficiencies of below 40%. This inefficiency stems from stringent requirements for temperature uniformity[2]. A promising solution lies in the utilization of textiles and innovative fibers to shift thermal regulation from the built environment to the microclimate surrounding the human body[3]. This approach enables the development of wearable personal thermal comfort systems (PTCS) that provide personalized thermal comfort and energy efficiency. Intelligent and functional fibers have shown great potential for a wide range of applications, including wearable devices and other high-tech fields[4–6].

[1]State Key Laboratory of Advanced Waterproof Materials, School of Materials Science and Engineering, Peking University, Beijing 100871, China. [2]College of Textiles, Donghua University, Shanghai 201620, China. [3]State Key Laboratory of Heavy Oil Processing, China University of Petroleum, Beijing 102249, China. [4]School of Advanced Manufacturing and Robotics, Peking University, Beijing 100871, China. [5]School of Advanced Materials, Peking University, Shenzhen Graduate School, Shenzhen 518055, China. ✉e-mail: qiningwang@pku.edu.cn; rzou@pku.edu.cn

Specifically, phase-change textiles (PTCs) have the potential to decouple human comfort from environmental conditioning by enabling localized microclimate regulation[7]. Phase-change materials (PCMs) can release and store heat at nearly constant temperatures, contributing to mitigating the issue of mismatch between constant temperature and thermal energy supply and demand[8,9]. Currently, organic PCMs such as paraffin wax, offer latent heat storage capacities of 200-300 $J \cdot g^{-1}$ while maintaining nontoxicity and commercial scalability[7,10]. Phase-change fibers (PCFs) are developed to absorb, store, and release heat in response to ambient temperature change[11]. This inherent property provides excellent temperature control and regulation capabilities, forming the foundation for the development of PTCs[3]. Smart clothing based on PTCs enhances human adaptability to external environmental conditions through effective energy storage and release[12]. However, despite their promising potential, several challenges hinder the industrial deployment of PCTs. Firstly, the low thermal conductivity less than 0.2 $W \cdot m^{-1} \cdot K^{-1}$ results in significant heat loss (40–60%) during phase transitions. Secondly, unconfined solid-liquid morphology instability leads to a 30–40% reduction in latent heat storage capacity. Moreover, poor solar absorptivity (<20%) limits their passive energy harvesting efficiency.

To address the problem of low thermal conductivity, high thermal conductivity fillers such as carbon fibers[13], carbon nanotubes (CNTs)[14,15], graphene[16,17], and nanoparticles are commonly used as additives to improve the thermal conductivity and promote the conversion of light/electricity to heat[18,19]. Additionally, nanoconfinement, chemical crosslinking, and polymer molding techniques have proven effective in mitigating solid-liquid phase transition leakage[20]. In particular, Jing et al.[21] reported a simple and cost-effective chemical crosslinking strategy to synthesize leak-proof, ultra-flexible, and thermally insulating polymer-based phase-change composites. This composite material features a unique dual three-dimensional (3D) crosslinked network of olefin block copolymer (OBC) and styrene-butylene-styrene (SEBS) in paraffin (PW). This innovative interaction enhances the brittleness and elasticity of material, leading to significantly improved flexibility. Specifically, the fracture strain increases from 23% to 560% while maintaining high latent enthalpy values[21]. This molecular chain network plays a crucial role in the efficiently encapsulating solid-liquid phase change materials, offering a promising pathway for green production of advanced composites with enhanced mechanical and thermal properties[22–24].

The common preparation methods for PCFs can be categorized into fiber filling, electrostatic spinning[25], wet spinning[11], and melt spinning[26]. Fiber filling is a simple and convenient method, involving the infiltration of PCMs into the pores of continuous hollow or aerogel fibers to endow them with a temperature-regulation function. However, sealing the end of the fiber remains challenging, and PCMs that infiltrate the pores are prone to being washed off during application, resulting in poor durability over cycles. Currently, the PCF technologies used in the market mainly focus on the microcapsule route with coatings or matrix immersion coatings, in which the enthalpy values of the obtained PCFs are limited, and the cycling durability is unsatisfactory. Electrospinning technology typically produces disordered fiber membranes and struggles to produce single continuous PCFs on a large scale[27]. Wet spinning, while scalable for industrialization, poses environmental concerns due to solvent evaporation during the process[11]. In contract, melt spinning is a clean method that does not require solvents and offers economic scalability for industrial products[26]. It is considered the most critical step in preparing continuous PCFs. Notably, the physical mechanism of melt spinning involves rapid cooling process of the molten polymer solution to induce solidification. The orientation of the molecular chains in the molten polymers contributes to the formation of more-ordered and stable solid-phase features. However, current approaches fail to achieve a balance between structural order and thermal regulation performance – a critical limitation given that 68% of wearable thermal failures are attributed to the microstructural instability of PCMs.

Here, we introduce a nanotechnology-inspired strategy that combines ultralow-CNT (0.1 wt.%) heterostructures with gradient crystallinity engineering to produce scalable PCFs. These fibers exhibit prominent synergy between thermal storage density ($\Delta H_m = 139.0\ J \cdot g^{-1}$, $\Delta H_c = 138.0\ J \cdot g^{-1}$) and adaptive thermal regulation capabilities. This strategy involves the creation of hierarchical three-dimensional interpenetrating polymer networks (3D-IPNs) using styrene-ethylene-butylene-styrene (SEBS) and high-density polyethylene (HDPE). These networks effectively confine n-docosane in a multidimensional nanostructure. The incorporation of CNTs (0.1 wt.%) serves as heterogeneous nucleation sites, enhancing both the orientation and mechanical properties through π-π stacking interactions. Molecular dynamics (MD) simulations validate these improvements (Supplementary Figs. 1–9). Compared with other chemical crosslinking and microcapsule methods, our dual-component melt-spun fibers demonstrate a significantly higher storage heat capacity (Supplementary Fig. 10). The fibrous architectures ensure defect-free textile processing, achieving cutting and sewing fidelity greater than 98%. Furthermore, the semi-automatic weaving of phase-change fabrics with an enthalpy of 87.6 $J \cdot g^{-1}$ enables smart garments to regulate body temperature by approximately 5 °C. This capability highlights significant potential for managing human thermal comfort in extreme environmental conditions.

Result

Fabrication strategy of PCFs and fabric

Figure 1 illustrates the manufacturing process with schematic representation and photographs of carbon-based phase change composites (referred to as C22/CNT@HDPE-SEBS) (Fig. 1a), carbon-based PCFs (referred to as C22/CNT fibers) (Fig. 1b, d, e), and PCM-based fabrics (referred to as CNT-PCTRFs) (Fig. 1c, f, and Supplementary Fig. 11). Additionally, it shows a smart thermoregulated phase-change garment (Fig. 1g). The multi-scale confined phase change composite, C22/CNT@HDPE-SEBS, incorporates a polystyrene-grafted ethylene-butene copolymer network (SEBS, Mw = 16.1 k) and high-density polyethylene (HDPE, Mw=20 k), which form interpenetrating polymer networks (IPNs). This IPNs structurally stabilize n-docosane (C22) within a carbon nanotubes (CNTs)-reinforced matrix. The composites exhibit rapidly absorb heat in high-temperature environments, release heat in low-temperature environments, and maintain a stable shape without leakage. The C22/CNT fibers were fabricated from C22/CNT@HDPE-SEBS precursor using melt-spinning technology. PCM-based fibers with varying amounts of CNTs (0.05, 0.1, 0.5, and 1.0 wt.%) designated as C22/CNT1, C22/CNT2, C22/CNT3, and C22/CNT4 fibers, respectively, were utilized in the fabrication of PTCs using semi-automatic weaving machines. Phase-change garments were fabricated through the utilization of commercially available cutting and sewing machinery to process PTCs. The manufacturing process involves the precise cutting of phase-change fabric panels, which are subsequently assembled into garments using standard commercial sewing techniques. The manufacturing process begins with the uniform dispersion of CNTs in the liquid phase of n-docosane through ultrasonic cavitation. Leveraging the strong compatibility between SEBS and n-docosane, a sequential melt-blending approach was employed to disperse SEBS in the C22/CNT composite liquid phase, yielding the C22/CNT-SEBS gel. To form the C22/CNT@HDPE-SEBS composite, HDPE was mixed with the C22/CNT-SEBS gel. This mixing step was conducted in an internal mixer at 175 °C for 45 minutes under atmospheric pressure. The resulting mixture was cooled and mechanically crushed into small particles, which were then processed via twin-screw melt spinning. The primary PCFs underwent uniform multistage stretching to obtain the final C22/CNT fibers. In this process, HDPE and SEBS polymer chains intertwine after two high-temperature mixing process, forming an IPNs

https://doi.org/10.1038/s41467-026-68951-x

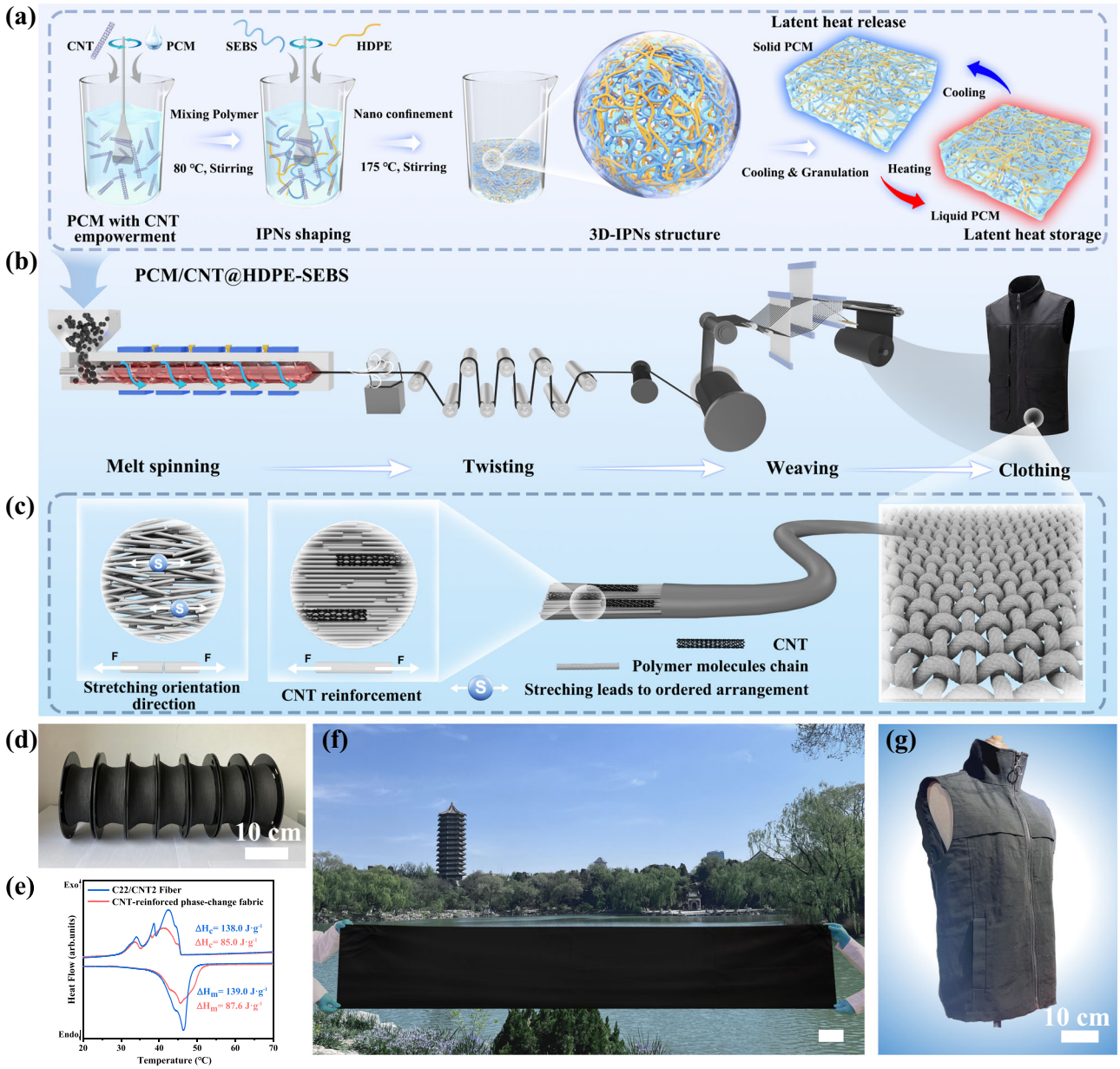

Fig. 1 | Illustration of the procedure for fabricating C22/CNT@HDPE-SEBS, C22/CNT fibers and PCM-based fabric. a The preparation flowchart of C22/CNT@HDPE-SEBS composite, (**b**) the production of C22/CNT fibers through bi-component melt-spinning, phase-change fabric and garments, (**c**) the influence of CNT on the orientation of phase change fibers, (**d**) a photograph of spooled CNT-reinforced PCFs produced by continuous spinning (**e**) crystallization enthalpy values and melting enthalpy values for the cooling and heating process curves of C22/CNT2 fibers, respectively. Similarly, crystallization enthalpy values and melting enthalpy values corresponding to the cooling and heating process curves of CNT-reinforced phase-change fabric, respectively, (**f**) a photograph of the CNT-reinforced phase change fabric with scale bar of 20 cm, and (**g**) a photograph of thermoregulated phase-change garments.

structure that tightly encapsulates the small molecules of the C22/CNTs liquid phase.

Specifically, the construction process of the multi-stage nano-confinement of the n-docosane-based composite fiber consisted of three steps. The first step is the nanoconfined encapsulation, where CNTs were uniformly dispersed in liquid n-docosane. And then, it involves 3D-IPNs reinforcement. At this stage, through sequential thermal blending at 175 °C for 45 min, dual polymer frameworks are formed. These frameworks crosslink physically via bi-continuous IPNs structures, enhancing the material's stability. Finally, it is melt-spinning-induced crystallization combined with twin-screw extrusion and multi-stage drawing (100–160 °C). This process aligns polymer chains and further nanoconfinements, crucial for achieving the desired material properties. After crosslinking, the molecular chains undergo cooling and multistage stretching, leading to nanoconfined encapsulation and traction shaping. The cavitation effect caused by the multiple stretching orientations of molecular chains, helps consolidate and stabilize n-docosane within the composite structure. The resulting stable IPNs architecture is characterized by the production of continuous PCFs.

To further investigate the influence of stretching cycling on the mechanical properties of the fibers, we designed and conducted a series of controlled experiments to isolate each processing stage and characterize its stage-specific crystallization behavior. DSC analysis unambiguously demonstrates a progressive enhancement in crystal perfection and crystal size from the masterbatch to the final fiber (Supplementary Fig. 12 and Supplementary Table 1). Furthermore, the XRD results indicate that the diffraction intensity systematically

increases with successive stretching steps, providing direct evidence of the structural evolution (Supplementary Fig. 13b). This demonstrates that the multi-stage stretching process is the dominant factor in achieving high molecular orientation, with an effect that substantially exceeds the preliminary alignment achieved by melt-spinning alone. This strongly demonstrates the dominant role of the stretching process in promoting further chain orientation, slip, and rearrangement, thereby facilitating the formation of a more perfected and stable crystalline structure. Moreover, compared to the as-spun fibers, the multi-stage stretching fibers exhibit remarkable increases in tensile strength and modulus of approximately 106.5% and 331.8%, respectively (Supplementary Fig. 14). These results collectively demonstrate that multi-stage stretching process promotes chain alignment and crystal perfection, thereby substantially enhancing mechanical performance.

However, initial stretching stage can effectively enhance CNT alignment and fiber densification, causing enhancement in mechanical strength (Supplementary Fig. 14b). But excessive stretching cycles may lead to CNT fracture and interface damage, ultimately degrading performance (Supplementary Fig. 14c). Thus, three stretching cycles determined are an optimal balance point for continuous collection between performance improvement and damage risk in our system.

In terms of material composition, n-docosane serves as the host material, retaining the high latent heat enthalpy of the composites. SEBS and HDPE, on the other hand, provide the composite with leakage-proof properties and mechanical strength. To determine the optimal proportions of the three components, a series of experiments was conducted to assess their impact on enthalpy and shape stability (Supplementary Fig. 15). The final mass ratio determined was 62.5 wt.% n-docosane: 11.25 wt.% SEBS: 26.25 wt.% HDPE (as detailed in Supplementary Fig. 15 and Supplementary Table 2). The developed phase-change composites demonstrate excellent structural stability and leakage-free performance, rendering them highly suitable for diverse applications. Leveraging the advantages of easy orientation induction, CNTs prove effective as reinforcing agents in fiber-reinforced composites (Fig. 1c).

To evaluate the influence of incorporating CNTs on PCFs properties, further experiments were conducted. The resulting CNT-reinforced PCFs demonstrate significant toughness, enabling their processing with commercial sewing equipment for stitching applications (Fig. 1f, g and Supplementary Fig. 11). This compatibility with existing textile manufacturing techniques facilitates the seamless integration of thermoregulatory CNT-reinforced PCFs into various garment architectures and woven configurations. Given these versatile properties, CNT-reinforced PCFs hold great promise for a wide range of clothing and textile designs.

Microstructure of C22/CNT fibers

C22/CNT fibers with varying CNTs contents were produced via continuous melt spinning. To examine the microstructures of the carbon-based PCFs, scanning electron microscopy (SEM) and transmission electron microscopy (TEM) were employed. As illustrated in Fig. 2, the appearance, microstructure, and morphology of the scalable single-roll C22/CNT3 fibers spools (outer diameter 200 mm, and inner width

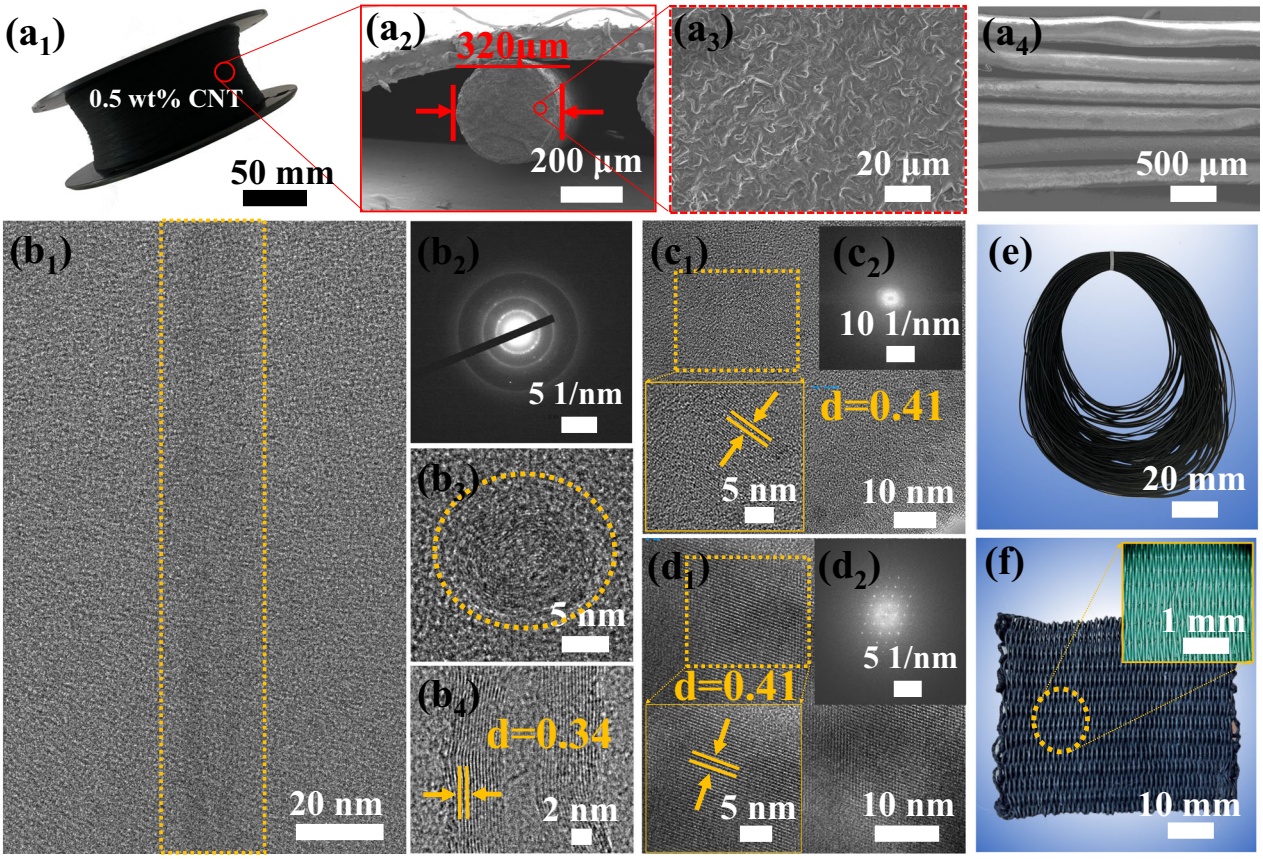

Fig. 2 | Structural characterization of C22/CNT3 fiber. $\mathbf{a_1}$ C22/CNT3 fiber images, ($\mathbf{a_2}$) and ($\mathbf{a_3}$) SEM cross-sectional images of C22/CNT3 fiber, ($\mathbf{a_4}$) SEM images of C22/CNT3 fiber. $\mathbf{b_1}$ and ($\mathbf{b_4}$) CNTs lattice fringes in the TEM image of the axial cross-section inside the C22/CNT3 fiber. $\mathbf{b_2}$ Lattice fringe and ($\mathbf{b_3}$) cross-section of CNTs inside the C22/CNT3 fiber. $\mathbf{c_1}$ and ($\mathbf{c_2}$) Lattice fringes of HDPE inside C22/CNT3 fiber. $\mathbf{d_1}$ and ($\mathbf{d_2}$) Lattice fringe of C22 inside C22/CNT3 fiber. **e**, **f** Images of primary C22/CNT3 fiber and CNT-PCTRFs (5 × 5 cm).

56 mm), primary C22/CNT3 fibers, and phase-change fabrics are clearly demonstrated. Detailed morphologies include cross-sectional, interfacial, local, and fiber surface morphologies (Fig. 2a_2–a_4), respectively. The micro- and cross-sectional surfaces of the C22 fibers exhibit a flat texture, indicating that n-docosane was effectively encapsulated within the polymer molecular chains (Supplementary Figs. 16–17). The incorporation of CNT caused a noticeable change in fiber color (Fig. 2a_1, Supplementary Fig. 18). The average diameter of the C22/CNT3 fibers was 320 μm, while the primary fibers have a diameter of 1 mm (Fig. 2e). The C22/CNT fibers originated from primary fibers that underwent multistage stretching. During this process, polymer molecular chains gradually aligned along the axial direction of the fibers, leading to a reduction in fiber diameter. Additionally, the cavitation effect induced by the stretching orientation further confined n-docosane and prevented leakage.

To investigate the structural characteristics of the fibers with CNTs, the fibers were sliced along the axial direction at a temperature of −340 °C. The ultra-thin sections obtained from the axially cut C22/CNT3 fiber exhibited a thickness range of 40–50 nm. Subsequently, the resulting samples were analyzed using high-power transmission electron microscopy (TEM) to examine the distribution of CNTs and their lattice structure. The CNT within the fibers could align along the axis direction as shown in Fig. 2b_1, b_2. The size of the CNT was determined to be 20 nm based on the electron diffraction pattern (Fig. 2b_3), with an interplanar spacing of a single lattice of 0.34 nm (Fig. 2b_4, and Supplementary Fig. 19). This provides strong evidence that the CNTs maintain their structural integrity within the composite. Furthermore, this finding is expected to have a favorable effect on both the thermal conductivity and mechanical properties of carbon-based PCFs. To further verify the crystalline structure of HDPE, we performed FFT analysis via GMS2 software on HRTEM images of the polymer matrix regions. The LiveFFT diffraction pattern clearly revealed two distinct diffraction spots corresponding to lattice spacing of 0.41 nm and 0.37 nm, with measured interplanar distance of 0.413 nm (Fig. 2c_1, c_2). These values show excellent agreement with the (110) and (200) planes of orthorhombic polyethylene, respectively, as established in literature[28]. This confirms unequivocally that the observed lattice fringes in this region originate from the crystalline phase of HDPE rather than other components. A monoclinic crystal system structure was attributed to the n-docosane component with a lattice spacing of 0.41 nm (Fig. 2d_1, d_2). Finally, as demonstrated in Fig. 2f, the manual weaving of carbon-based phase-change fabrics is a viable approach for fabricating these materials.

Thermophysical properties of C22/CNT fibers and their crystallization mechanism with minimal CNT loading

The phase change enthalpy of composite materials plays a significant role in energy density within thermal storage systems. Different scanning calorimetry (DSC) analysis revealed that phase transition stability of C22/CNT fibers is up to 62.5 wt% n-docosane loading without leakage, with enthalpy values ($\Delta H_m = 139.0\ J{\cdot}g^{-1}$, $\Delta H_c = 138.0\ J{\cdot}g^{-1}$ at 0.1 wt.% CNT), surpassing conventional melt-spun fibers (Fig. 3a–d and Supplementary Fig. 20 and Supplementary Table 3). This enhancement attributed to the regular arrangement of the molecular chains and the induced crystal growth. The introduction of CNTs increased the thickness and size of n-docosane crystals, thereby elevating both enthalpy and phase transition temperature in the C22/CNT fibers. The incorporation of a small amount of CNTs acted as a nucleating agent, facilitating the nucleation and crystallization of n-docosane. However, excessive CNTs can lead to entanglement and aggregation, disrupting the crystal structure of n-docosane and reducing the enthalpy value of the C22/CNT fibers. To evaluate the thermal storage capability of the C22/CNT fiber, we use Eq. (4) (Supplementary Table 3). All samples exhibited value of $C\%$ exceeding 99%, indicating effective encapsulation and reliable phase transition for latent heat storage and release. Thermal reliability was further validated through accelerated cycling tests (Fig. 3b, Supplementary Figs. 21–22, and Supplementary Table 3) and thermogravimetry measurement (Supplementary Fig. 23). The onset decomposition temperature increased by 10 °C to 222.0 °C (Supplementary Fig. 23), confirming PCFs stability. The addition of CNTs significantly enhanced PCFs thermal conductivity by 715%, from $0.13\ W{\cdot}m^{-1}{\cdot}K^{-1}$ to $1.06\ W{\cdot}m^{-1}{\cdot}K^{-1}$ (Supplementary Fig. 24). This improvement enables rapid heat transfer via axial CNT networks, ensuring efficient energy exchange.

The crystallization properties of the C22/CNT fibers were characterized using a wide-angle X-ray scattering (WAXS) structure analyzer. The diffraction patterns of pure n-docosane and HDPE were fully replicated in the C22/CNT2 fibers, indicating no chemical interaction within the composite system (Fig. 3c). Furthermore, in-situ XRD studies (Supplementary Figs. 25, 26) and polarization optical microscopy (POM) studies (Supplementary Figs. 27, 28) revealed confined n-docosane crystallization within the 3D-IPNs, effectively suppressing liquid leakage during phase transitions. Furthermore, the integration of CNTs was found to reduce both melting and crystallization temperature, which is advantageous for accelerating crystal nucleation kinetics (Supplementary Fig. 28). A comparative analysis of PCFs fabricated via melt spinning, wet spinning, and electrospinning methods, based on an extensive literature review, demonstrated that the carbon-based PCFs developed in this study exhibited excellent enthalpy properties with the phase change efficiency exceeding 99% ($C\% > 99$, Supplementary Table 3) (Fig. 3d). This hierarchical confinement strategy represents a significant advancement for wearable thermoregulation textiles by integrating high-energy-density PCMs with nanotechnology-enabled thermal conductivity.

Full molecular dynamics (MD) simulations were performed to investigate the effects of CNT incorporation on the crystallization behavior of n-docosane. The MD simulations revealed a concentration-dependent regulation mechanism of n-docosane crystallization by CNTs (Fig. 3e–g): at low CNT loadings (0.1 wt%), surface interactions facilitated heterogeneous nucleation, significantly accelerating crystallization kinetics— from 50 ps in the composite system compared to 100 ps for pristine n-docosane — while maintaining large crystalline domains (Fig. 3f and Supplementary Fig. 29). In contract, a higher CNT concentrations (>0.5 wt.%), the formation of percolating networks restricted molecular mobility, leading to a reduction in overall crystallinity (Fig. 3g). These findings highlight a dual-mode concentration dependence of CNTs, underscoring the pivotal role of tunable performance under varying conditions.

During crystallization, molecular chains undergo sequential movements and conformational changes to achieve ordered arrangement. These transformations are essential for the crystallization process. As shown by the two-stage mean square displacement (MSD) dynamics (Fig. 3h), the crystallization mechanisms are controlled by CNT concentrations. In the initial stage of crystallization, MSD increases with time, indicating enhanced molecular mobility and conformational dynamics. The steep growth slope suggests that molecular chains exhibit high mobility, undergoing numerous structural rearrangements to extend their lengths and form locally ordered domains. Subsequently, MSD growth slows down until it approached a plateau, reflecting reduced chain mobility as the system transitions toward long-term ordering. High-CNT systems (>0.5 wt.%) exhibited 3× faster MSD growth rates in the initial stage (0–20 ps) compared to low-CNT system (0.1 wt.%). This acceleration is attributed to increased interfacial interactions between CNTs and polymer chains, which enhances chain mobility and alignment (Supplementary Fig. 29). The formation of crystal nuclei is facilitated by these enhanced interfacial interactions, with molecular chain extension becoming more pronounced. However, at higher CNT concentrations (>0.5 wt.%), the interconnected CNT networks restrict segmental motion in the later

https://doi.org/10.1038/s41467-026-68951-x

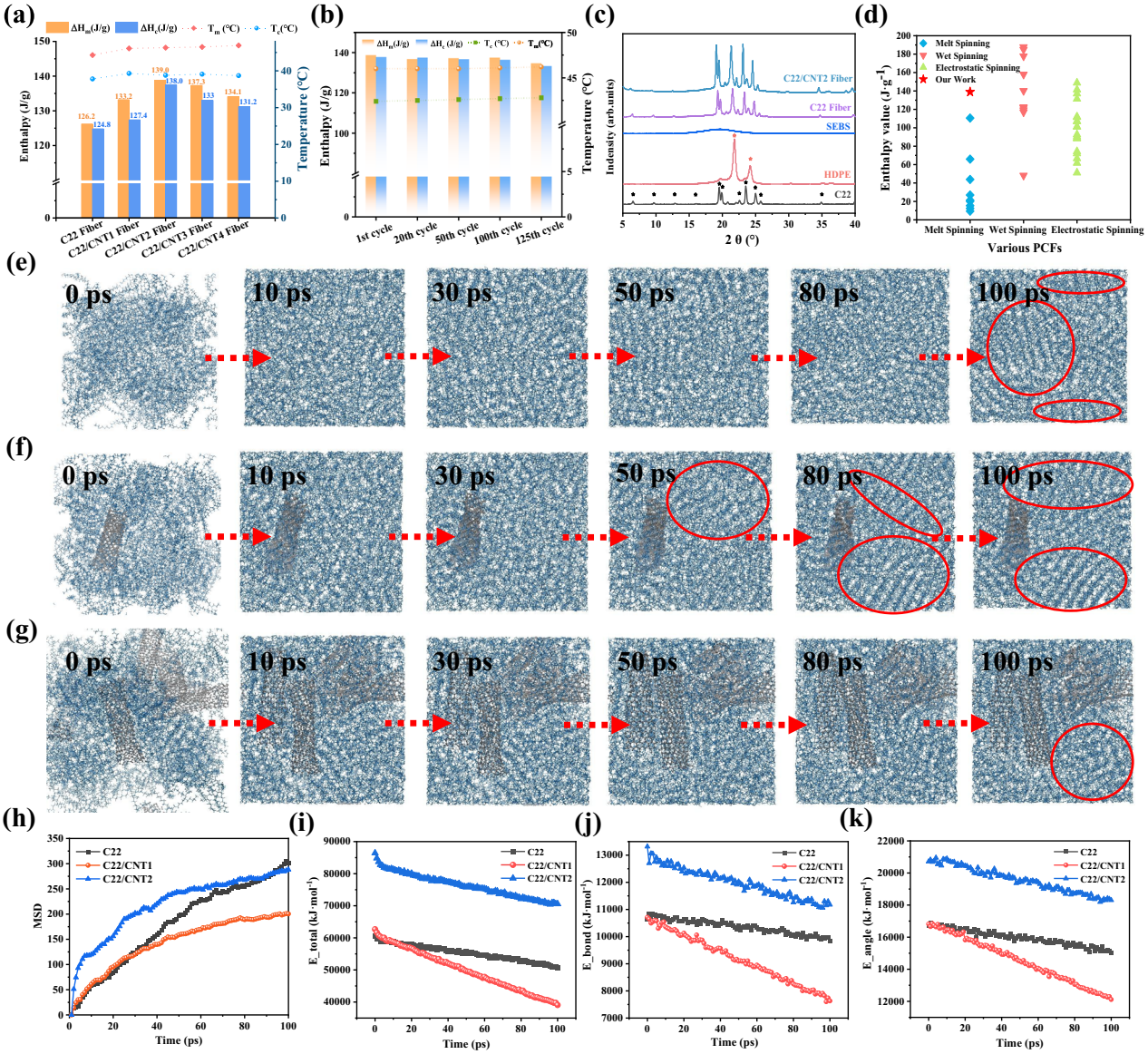

Fig. 3 | Thermal properties of C22, HDPE, SEBS, and C22/CNT fibers, MD analysis of the induced crystallization mechanism of CNTs during crystallization. a Enthalpy and phase-change temperatures of C22 fibers with varying amounts of CNTs. **b** Enthalpy and phase-change temperature of C22/CNT2 fibers after the 1st, 20th, 50th, 100th, and 125th accelerated thermal cycles. **c** Powder X-ray diffraction (XRD) of C22, HDPE, SEBS, C22 fiber, and C22/CNT2 fiber. **d** Property distribution of the different types of PCFs was examined in terms of toughness and latent heat storage capacity[12,26,27,31–65]. MD snapshots of the crystallization process of: (**e**) n-docosane, (**f**) n-docosane with one CNT (denoted as C22/CNT1, 0.1 wt.%), and (**g**) n-docosane with six CNTs (denoted as C22/CNT2, > 0.5 wt.%) at 0 ps, 10 ps, 30 ps, 50 ps, 80 ps, and 100 ps, respectively. **h** Mean square displacement of the system during crystallization. Variations in potential energy (**i**), bond energy (**j**), and angle energy (**k**) of the phase-change composite system over time during the cooling process.

stage (20-80 ps), as evidenced by slower MSD growth rates compared to low-CNT systems (Supplementary Fig. 29). This restriction arises from the increasing hindrance imposed by the filler network, which slows down chain mobility and ultimately affects crystal nucleation, as well as the overall crystal structure and region size of the system.

The total potential energy of each microscopic particle in the system is determined by its spatial position and describes the macroscopic thermophysical properties of the material. In MD simulations, changes in free energy are typically derived from variations in molecular potential energy. A statistical analysis of the potential energy composition of the composite system was conducted during the crystallization process (Fig. 3i–k and Supplementary Fig. 30). The total potential energy (E_{total}), bond stretching energy (E_{bond}), bond angle bending energy (E_{angle}), dihedral torsional potential energy ($E_{torison}$), and interfacial interaction energy (E_{inter}) which characterize intermolecular interaction in the composite phase transition system, exhibiting a linear decreasing trend as crystallization processed. In contrast, nonbonding interaction energy (E_{vdw}) remained relatively constant. The system with low CNT loading achieves a markedly lower interfacial energy during crystallization, as evidenced by its rapid decrease in Supplementary Fig. 31a. This suggests that a small amount of CNT provides a low-energy interface for n-docosane. At this moment, the nucleation barrier for heterogeneous crystallization, which is governed by the interfacial energy term, becomes significantly lower than that for homogeneous nucleation according to the heterogeneous nucleation theory[29]. Furthermore, the synergistic decline in both E_{angle} and $E\_{torsion}$ (Supplementary Fig. 31b) indicates that the molecular segments integrate into the crystal lattice with minimal

https://doi.org/10.1038/s41467-026-68951-x

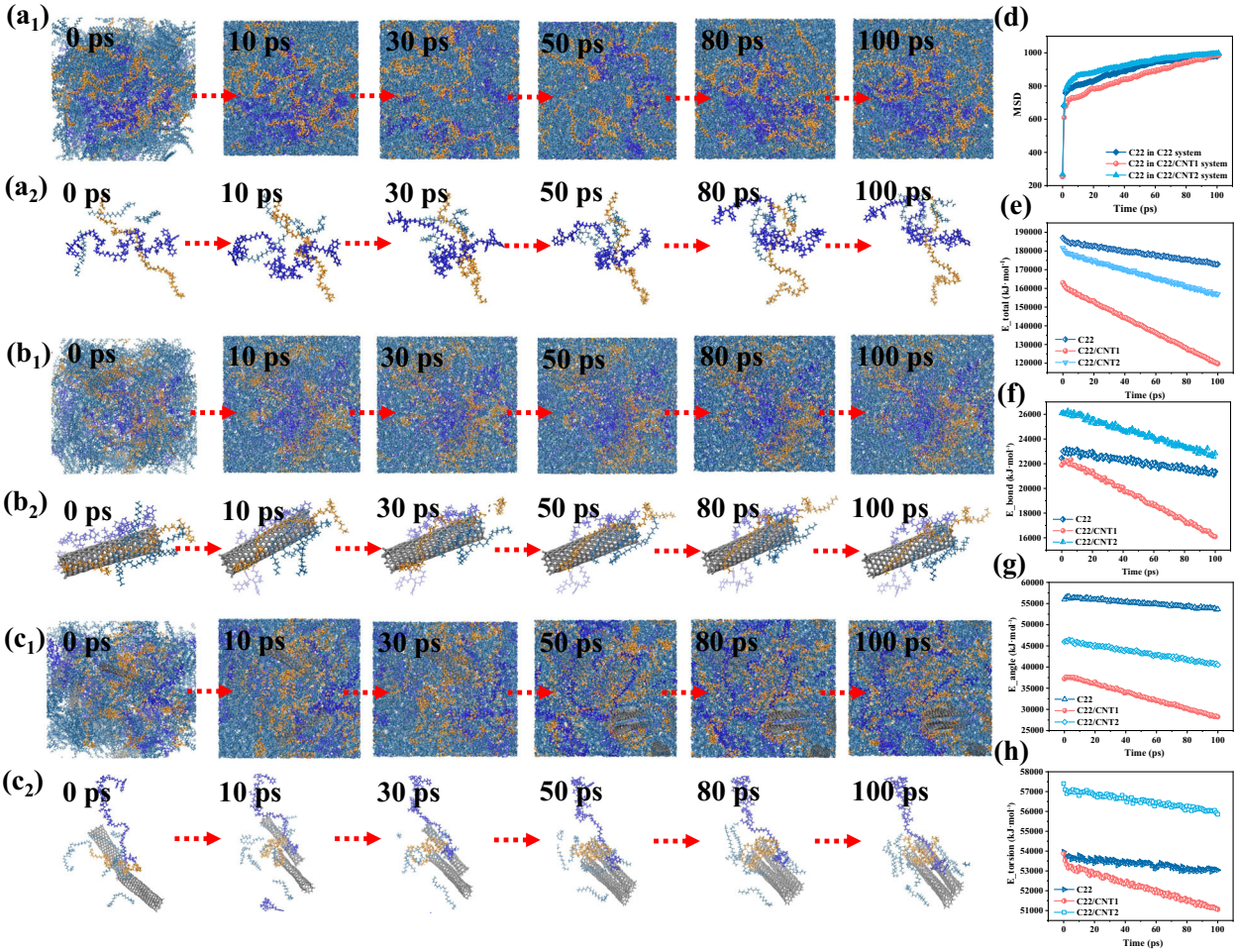

Fig. 4 | MD analysis of the induced crystallization mechanism of CNTs during crystallization in the comprehensive full-component systems. MD snapshots (**a_1**–**c_1**) and the corresponding local area (**a_2**–**c_2**) of the crystallization process of: (**a_1**, **a_2**) SEBS-HDPE-n-docosane, (**b_1**, **b_2**) SEBS-HDPE-n-docosane with three CNT (denoted as C22/CNT1, 0.1 wt.%), and (**c_1**, **c_2**) SEBS-HDPE-n-docosane with eighteen CNTs (denoted as C22/CNT2, >0.5 wt.%) at 0 ps, 10 ps, 30 ps, 50 ps, 80 ps, and 100 ps, respectively. **d** Mean square displacement of n-docosane within different full-component systems during crystallization. Variations in potential energy (**e**), bond energy (**f**) angle energy (**g**), and torsion energy (**h**) of the comprehensive full-component systems over time during the cooling process.

conformational adjustment in low-CNT loading system. MD snapshots visually confirm this phenomenon: in the low-CNT loading system, n-docosane molecules adsorbed on the CNT surface undergo only subtle conformational adjustment (Fig. 3e, f and Supplementary Fig. 32ab). A small lattice mismatch exists between the CNT and the crystal, thereby suppressing lattice distortion during the growth of the nucleus and facilitating the formation of a low-strain nucleus. This strain energy relief facilitates a rapid nucleation rate by lowering the energy barrier for stable nucleus formation. In contrast, the system with excessive CNT loading induces significant conformational rearrangement of n-docosane at the interface due to stronger interfacial interactions (Fig. 3g and Supplementary Fig. 32c). Thus, a small amount of CNTs functions as heterogeneous nucleating agents by progressively lowering the interfacial energy and inducing a pre-ordered structure (which reduces strain energy), thereby mitigating molecular-level energy barriers. Thus, free energy analysis revealed that CNT-induced nucleation barrier reductions in nucleation barriers were attributed to decreases in interfacial energy and strain energy minimization.

The incorporation of CNTs caused the formation of an additional phase interface, which reduced the surface tension and energy barrier necessary for nucleation (i.e., the critical nucleation-free energy). The phase transition from the liquid to solid state was accompanied by a reduction in the intermolecular distance, a linearly decreased in bond-stretching energy, and an increase in the compactness of the molecular structure within the system. The hierarchical 3D-IPNs confinement regulated the CNT network formation, balancing nucleation enhancement at low CNT concentrations and mobility restriction at high CNT concentrations. This dual-mode dependence on CNT concentration aligns with the industrial requirements for adjustable crystallization kinetics in thermoregulation textiles.

To further investigate the crystallization process in the realistic sample situation, three comprehensive full-component systems models including SEBS-HDPE-C22, SEBS-HDPE-C22-3CNT (0.1 wt% CNT loading), SEBS-HDPE-C22-18CNT (> 0.5 wt.% loading) were constructed for simulation. Across all three full-component systems, MD snapshots and corresponding local areas showed no emergence of ordered n-docosane arrangements during crystallization (Fig. 4$a_1a_2b_1b_2c_1c_2$), confirming that SEBS and HDPE spatially confine n-docosane. Furthermore, while serving as a structural scaffold, these polymers effectively prevent n-docosane leakage – behavior fully consistent with the morphological stability observed in our experiments. Despite this confinement, we clearly observed that in the presence of CNTs, both the molecular chains of polymer and n-docosane are co-adsorbed onto the CNT surface (Fig. 4$b_1b_2c_1c_2$). Initially characterized by a disordered atomic arrangement, the interface of molecular chain and CNT

exhibits high interfacial energy and considerable local strain (Supplementary Fig. 33). As crystallization proceeds, crystalline nucleus emerges on the CNT surface, displaying a well-defined epitaxial match with the CNT lattice in the low-CNT loading systems, which is different from the initial state.

This indicates that molecular chains are rapidly adsorbed onto the CNT surface with only subtle conformational adjustment, forming a pre-oriented layer in the low-CNT loading system (Fig. 4b_1b_2). In contrast, the system with excessive CNT loading induces significant conformational rearrangement of molecular chains at the interface due to strong interfacial interactions (see Fig. 4c_1c_2). This finding demonstrates that a small amount of CNTs remain potent heterogeneous nucleating agents even within complex multicomponent environments, thereby validating the universality and reliability of the core mechanism identified by our initial model.

Compared to the initial model, analysis of the mean squared displacement (MSD) curves for different components across the three full-component systems reveals that although n-docosane, HDPE, SEBS exhibit relatively high initial diffusion rates, their overall dynamics are ultimately compromised used to constraints imposed by the cross-linking network of polymer molecular chains (Fig. 4d and Supplementary Fig.34). Furthermore, in higher CNT loading system, the formation of percolating network restricted molecular mobility, leading to a reduction in overall crystallinity. In contrast, in low-CNT loading system, the diffusion rates of SEBS and HDPE remained comparable to those in the pure C22 system, while the MSD curves of n-docosane molecules indicated rapid condensation (crystallization) induced by CNTs. This kinetically confirms that a low CNT concentration can efficiently guide the ordering of n-docosane molecules.

Furthermore, we performed a comprehensive analysis of the total potential energy, bond energy, non-bonded interaction energy, and interfacial interaction energy of three full-component systems during the crystallization process (Fig. 4e–h, and Supplementary Fig. 33). The results demonstrated that the system with low-CNT loading exhibits the most rapid decrease in energy (including $E_{\_total}$, $E_{\_bond}$, $E_{\_angle}$, $E_{\_torsion}$, $E_{\_inter}$) and achieves the lowest final energy state, indicating the most stable configuration (Fig. 4e–h, and Supplementary Fig. 33). This provides compelling thermodynamic evidence that this system forms a more stable crystalline structure, unequivocally highlighting the significant advantage of a small amount of CNT as a heterogeneous nucleating agent in reducing the nucleation barrier and promoting overall system stability.

These MD simulation results of comprehensive full-component models are fully consistent with the conclusions from our initial simplified model. The simplified model successfully isolated and revealed the heterogeneous nucleation mechanism induced by a small amount of CNT, while the full-component model validates the effectiveness of this mechanism under realistic conditions, while additionally revealing the confinement effects imposed by the polymer components.

Mechanical properties of C22/CNT fibers and orientation enhancement mechanism of CNTs

The mechanical behavior of PCFs is critical for their performance in thermal energy storage systems, requiring a delicate balance between strength and ductility. Conventional polyolefin-based PCFs exhibit inherent brittleness due to n-docosane chain immobilization (Supplementary Fig. 35), with tensile strength to 5.6 MPa and fracture toughness of $28 \pm 10\ MJ{\cdot}m^{-3}$ constrained by polymer chain disentanglement. In contrast, our CNT-engineered C22/CNT fibers demonstrated a concentration-dependent reinforcement regime (Fig. 5a, b), achieving significant synergy between ductility and strength through hierarchical microstructural control. The tensile strength of the C22/CNT fibers reached a maximum value of 8 MPa with the incorporation of 1.0 wt.% CNTs, representing a significant improvement over the 5.6 MPa tensile strength of pure C22 fiber. Additionally, the elastic modulus of C22/CNT fibers (780 MPa at 1.0 wt.% CNT) exhibited a slight increase compared to pure C22 fibers (700 MPa) (Fig. 5a). The elongation at break of the C22/CNT fibers reached a maximum value of 1652% when 0.05 wt.% CNTs were added, representing a 147% increase compared to C22 fibers (669 %). However, further increases in CNT content led to a decrease in elongation at break, which eventually became lower than that of pure C22 fibers when the CNT content exceeded 0.5 wt.%. Furthermore, the work of fracture of C22/CNT fibers initially increased with CNT addition, reaching a maximum value of $130 \pm 10\ MJ{\cdot}m^{-3}$ at 0.5 wt.% CNTs—a 365% improvement compared to pure C22 fiber ($28 \pm 10\ MJ{\cdot}m^{-3}$) (Fig. 5b). These observations suggest that the addition of a small amount of CNTs can significantly enhance the mechanical properties of PCFs. The n-docosane in the composite plays a critical role in improving CNT dispersion via infiltration effects, facilitated by its high affinity for carbon nanotubes. This interaction promotes effective stress transfer between the CNTs and polymer chains, resulting in excellent dispersion and improved mechanical performance. However, as the CNT content increases beyond optimal levels, the likelihood of defect formation within the fibers becomes significant. This inhibitory effect on reinforcement outweighs the beneficial effects of CNT addition at higher concentrations, ultimately limiting further improvements in mechanical properties. The ultra-high efficiency of CNTs in enhancing fiber toughness demonstrated by a minimal addition achieving remarkable improvements in elongation at break highlights their potential as a highly effective reinforcement agent for PCFs.

The mechanical reinforcement in C22/CNT fibers originates from CNT-modulated crystallization kinetics and chain orientation dynamics of the polymer matrix. In-situ SAXS/WAXD characterization (Fig. 5c and Supplementary Figs. 36–40) reveals a concentration-dependent dual-phase reinforcement mechanism. As the degree of stretching increases, the radius of the special diffraction rings decreases concomitantly with increasing strength, indicating an increase in the orientation of the molecular chains (Supplementary Fig. 37). This reflects the tendency of the molecular chains to become more ordered and oriented upon stretching. To further investigate the chain orientation differences in PCFs, azimuth information was analyzed (Supplementary Fig. 38). Fibers tend to deform along the direction of external forces. In-situ 2D-WAXD analysis shows that incorporating a small amount of CNT enhance the chain orientation arrangement of during stretching at the same deformation level (700%) (Supplementary Fig. 39). A narrower full width at half maximum (FWHM) corresponds to a higher degree of fiber orientation. The 2D-WAXD images of C22/CNT1 fibers, combined with disparities in FWHM and chain orientation between C22 fibers and C22/CNT1 fibers, confirm the improved stretching orientation and crystallization of C22/CNT1 fibers. This indicates that introducing 0.05 wt% CNTs promotes polymer chain arrangement (Fig. 5c). As the deformation increases gradually, fiber orientation enhances and ultimately stabilize before fracture occurs (Fig. 5d). Notably, the incorporation of CNT within the range of 0.05 wt.% to 0.1 wt.% exerted a substantial effect on the orientation of the fibers (Supplementary Fig. 40), aligning with findings of the mechanical experiments.

However, under lower CNT loading conditions (0.05 wt.%), CNTs are primarily individually dispersed, which facilitates their uniform distribution within the polymer matrix and allows then to be sufficiently wetted by the polymer. Thus, these individually dispersed CNTs can more readily align along the direction of shear or tensile flow during melt processing. The stretching process further facilitates the alignment of these well-dispersed, low-content CNTs along the stretch direction, yielding a high degree of orientation. This high orientation, combined with good dispersion, is pivotal for efficient stress transfer.

When the CNT content increases to 0.1 wt.%, the intensified van der Waals interactions between CNTs promote the formation of local

https://doi.org/10.1038/s41467-026-68951-x

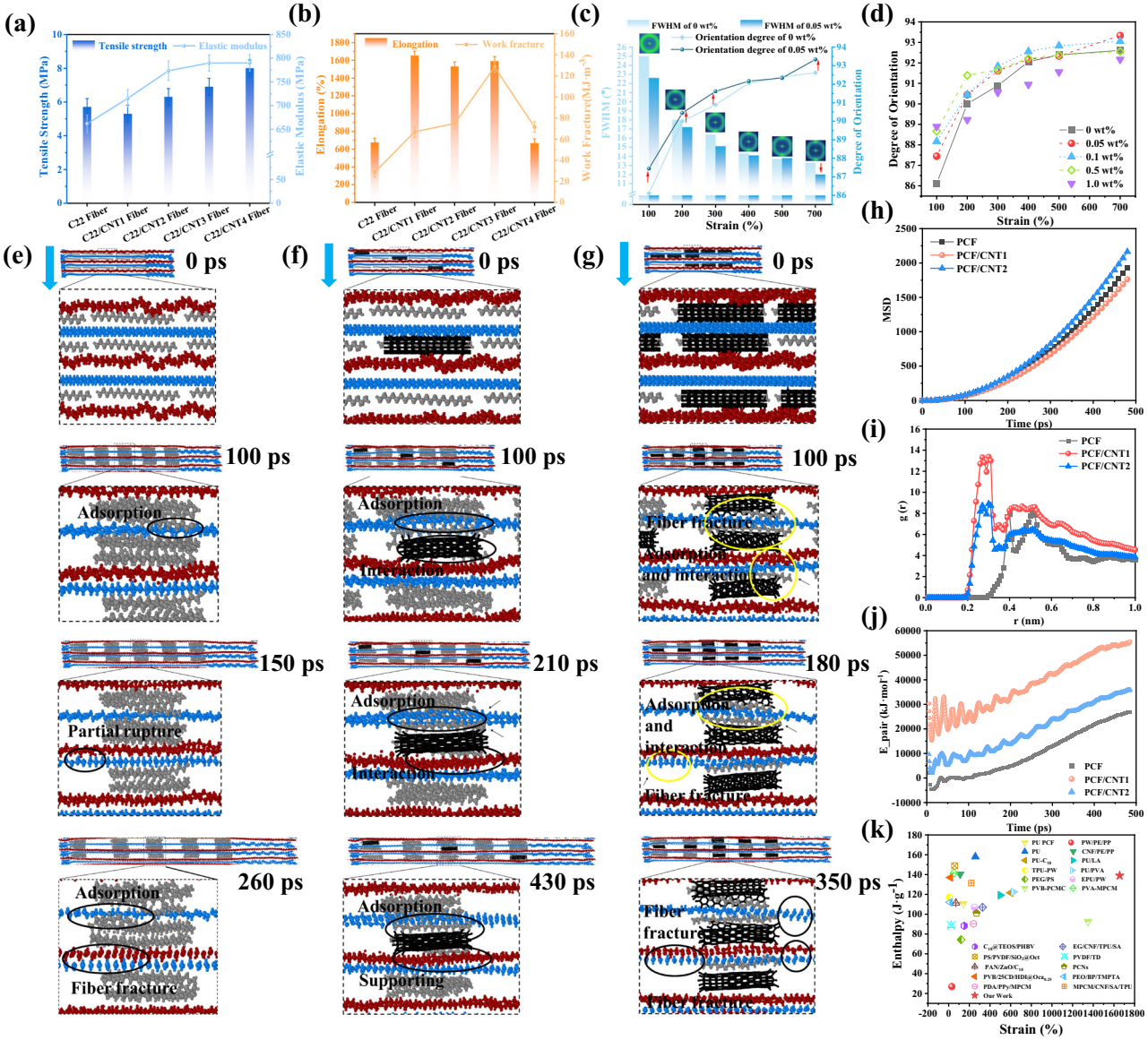

Fig. 5 | Mechanical properties and MD analysis of the orientation enhancement mechanism of C22 fibers with varying CNTs contents during the stretching process. a Comparison of the tensile strength and elastic modulus of C22 fibers with varying CNTs contents. Data are presented as mean values ± SD, $n = 3$ independent experiments. **b** Comparison of the elongation at break and toughness of the C22 fibers with different CNT contents. Data are presented as mean values ± SD, $n = 3$ independent experiments. **c** Comparison of the orientation degree, 2D-WAXS images, and FWHMs of the C22 fiber and C22/CNT2 fibers derived from in-situ 2D-WAXS analysis. **d** Comparison of the orientation degree of C22 fibers with varying CNTs contents at different stretching extents. MD snapshots of the stretching process of (**e**) C22 fibers at 0 ps, 100 ps (stretching state), 150 ps (partly factured state), and 260 ps (completely factured state), (**f**) C22 fibers with 6 CNTs (denoted as PCF/CNT1, 0.1 wt.%) at 0 ps (initial state), 100 ps (stretching state), 210 ps (stretching state), and 430 ps (completely fractured state), and (**g**) C22 fibers with 18 CNTs (denoted as PCF/CNT2, >0.1 wt.%) at 0 ps (initial state), 100 ps (stretching state), 180 ps (partly fractured state), and 350 ps (completely fractured state), respectively. **h** Mean square displacement curves. **i** Radial distribution function g(r) curves over time during the stretching process. **j** Variations in the non-bonding interaction energy of different phase-change composite fiber systems over time during the stretching process. **k** Property distribution of the different types of PCFs evaluated based on toughness and latent heat storage capacity[12,27,32,33,39–43,45–51,53–55,59,61–65].

aggregates. This promotes the formation of a robust percolating network, acts as enhanced physical cross-links and thermal barriers within the composites, contributing to enhancing thermal stability and mechanical strength (e.g., higher tensile strength and modulus). Furthermore, the denser CNT network provides a sufficient number of uniform nucleation sites, promoting more perfect overall crystallization. As suggested by Valentini[30], the heterogeneous nucleation efficiency of CNTs does not increase linearly with their content but rather exhibits a saturation behavior. An insufficient amount (e.g., 0.05 wt.%) offers too few sites to maximize this effect, while an excessive amount may hinder crystal perfection due to spatial confinement. Thus, although some local aggregation occurs, slightly reducing local orientation degree, the network effect outweighs the detriment, delivering the best balance of strength, thermal properties and latent heat. In short, the 0.05 wt.% CNT loading represents the microstructural threshold for optimal dispersion, maximizing the "single-fiber toughening effect", whereas 0.1 wt.% activates the "three-dimensional network enhancement effect", optimizing the trade-off between strength, thermal stability, and laten heat. For our target application – phase change fibers requiring reliable thermal

performance, energy density, and load-bearing capacity – the 0.1 wt.% CNT loading was selected as the system-wide optimum.

MD simulations revealed the formation mechanisms influenced by CNT concentration in polymer fiber systems. Under tension, the orientation of the molecular chains tends to align along the same direction (Fig. 5e-g). During the initial stretching process, the n-docosane crystal blocks gradually penetrated the polymer microfibers along the stretching direction (Fig. 5e). Within the microfibers, these crystal blocks were arranged in a stacked configuration and interconnected by taut-connecting molecules. The presence of voids between molecular chains is considered a primary factor contributing to defect formation within the fiber. Compared to polymers, CNTs exhibit noticeable orientation capacity during stretching. Consequently, they can be employed as orientation seeds for C22 fibers[16,20]. This property makes them effective as orientation seeds for aligning n-docosane small molecular and polymer chains, thereby reducing void formation and porosity. During stretching, the CNT axis aligns along the stretching direction, with interface region segments aligning along the CNT axis (Fig. 5f, g). These segments are influenced by two orientation effects: the CNT-induced orientation and the stretching-induced orientation. Additionally, the likelihood of interactions between multiple CNTs and individual molecular chains increases during stretching. This leads to segment adsorption by discrete CNTs, resulting in molecular chain bending.

During the stretching process, CNTs are gradually adsorbed onto the surface of n-dodecane and polymer molecular chains, causing the grain boundary area to gradually increase (Fig. 5f, g). The tortuosity of the grain boundaries inversely correlates with their ability to act as sites for fracture nucleation and microcrack propagation. At low CNT loadings (0.1 wt.%), CNTs function as physical crosslinks within the polymer matrix, enhancing network connectivity and tensile strength (Supplementary Figs. 41-42). However, above this threshold, CNT self-assembly forms percolating networks that restrict polymer chain mobility and create stress concentration points. These networks enhance stress distribution, promote grain refinement through heterogeneous nucleation, and reduce plastic deformation localization. As a result, the deformation becomes more uniform, stress concentrations are reduced, and fiber toughness is improved.

MSD analysis revealed distinct chain dynamics (Fig. 5h, and Supplementary Fig. 43), with all systems showing stress-induced chain mobility enhancement. However, the PCF/CNT1 system exhibited a lower MSD value, which correlated with the anisotropic chain reorientation and interfacial CNT-polymer attraction. During stretching, the alignment of CNTs along the loading direction facilitated the orientation of the molecular chain segments in the interfacial region, and thereby affecting the mobility of the molecular chains and increasing fiber flexibility. The density distribution map further highlights distinct reinforcement mechanisms (Supplementary Fig. 44). At low CNT loading (0.1 wt.%), enhanced interfacial adhesion restricted segmental motion while promoting lateral chain alignment, redistributing stress concentration to enhance mechanical toughness. In contrast, at high CNT loadings (>0.1 wt.%), CNT-induced percolation led to entanglement formation, creating localized stress zones that reduced fracture strain.

As shown in Fig. 5i, the radial distribution functions (RDF) of PCF/CNT1 and PCF/CNT2 exhibited distinct strain-dependent evolution. As tensile deformation proceeds, the g(r) values of the composite system increase gradually, concurrently with a narrowing of the g(r) distribution along the radial distance. This trend indicates that polymer chains and CNT become highly oriented in the stretching direction, promoting crystallization and a significant enhancement in structural order, thereby leading to the formation of ordered structure. Notably, PCF/CNT1 exhibited a stronger peak intensity than PCF/CNT2, attributed to its stronger interfacial adhesion at low CNT loadings, which preferentially highly aligned polymer chains along the loading axis. In contrast, excessive CNT loading causes chain entanglement, which may disrupt the oriented arrangement and reduce fracture toughness. Besides, the progressive strain led to RDF peak broadening and intensity decay in both systems, reflecting a transition from ordered chain alignment to disordered entanglement-dominated morphology. Strikingly, despite its lower CNT content, PCF/CNT1 exhibited greater strain-induced orientation than PCF/CNT2. This highlights the critical role of interfacial percolation in directing polymer chain organization and achieving enhanced material performance.

To elucidate the interfacial dynamics between the polymer matrices and CNTs during mechanical stretching, we analyzed the strain-dependent potential energy evolution (Fig. 5j). The CNT-engineered PCFs exhibited a higher energy absorption capacity than the neat fibers, attributed to shear-yielding deformation-induced interfacial friction. Leveraging the high specific surface area of CNTs, minimal loading suffices to generate interface-dominated phases, significantly enhancing energy dissipation efficiency. This interfacial percolation effect facilitated two synergistic mechanisms, including energy barrier modulation caused by CNT-matrix adsorption, which delayed disentanglement kinetics while promoting stress redistribution, and strain-induced crystallization, which reduced chain entropy via oriented packing. As a result, the energy levels of the molecular chains exhibited a tendency to increase and then decrease (Supplementary Fig. 45).

The entanglement of polymer chains with minimally loaded CNTs constrained the chain motion, forming a reinforced network. The confinement effect reduced defect densities, enhanced interfacial interaction, and induced an increase in axial sliding resistance, while enhancing tensile strength (σ = 6.32 MPa) and toughness (ε = 1530 %). The aligned CNT networks enhanced phonon transport while mitigating stress concentration during the stretching process. The hierarchical CNT-reinforced architecture resolved the trade-off between thermal stability (ΔH_m = 139.0 J·g^{-1}, ΔH_c = 138.0 J·g^{-1}) and mechanical performance through 3D-IPNs, surpassing the reported melt-spun (MS), wet-spun (WS), and electro-spun (ES) counterparts (Fig. 5k). This strategy establishes a universal design principle for developing wearable high-performance thermal energy storage systems in military and aerospace applications, where stringent demands exist for concurrent energy density, mechanical robustness, and thermal stability.

Solar energy utilization and wearable human thermal management

The development of carbon-based PCFs have led to the creation of innovative textiles capable of regulating temperature effectively. These fabrics are crafted using weaving and sewing technologies, as demonstrated in Fig. 1f and Supplementary Fig. 11, with garments prototype showcased in Fig. 1g. The key achievements include noticeable photothermal energy harvesting, high fidelity in phase change, and remarkable mechanical robustness. To assess the photothermal conversion performance, the corresponding measurements were conducted under simulated sunlight. Fabrics with varying CNT contents (denoted as CNT-PCTRFs) were evaluated, revealing that increasing CNT content enhances efficiency. Notably, fabric with 0.1 wt.% CNT achieved a temperature of 66 °C and an efficiency of 67.1% under 80 mW·cm^{-2} simulated sunlight, significantly outperforming the pristine fabric. The maximum temperatures recorded for the samples PCTRF, CNT1-PCTRF, CNT2-PCTRF, CNT3-PCTRF, and CNT4-PCTRF (with CNT contents of 0, 0.05, 0.1, 0.5, 1.0 wt.%) were 40, 66, 58, 60 and 63 °C, respectively (Fig. 6a). The photothermal conversion and storage efficiency (η) of CNT-PCTRFs exhibited a dose-dependent enhancement as the CNT loading increased. Specifically, η rose from 34.5% to 67.1% when the CNT content was increased from 0 to 1.0 wt.% under an isoflux condition of 80 mW·cm^{-2} (Supplementary Fig. 46). Notably, the CNT4-PCTRF achieved a photothermal conversion efficiency of 67.1%, which outperformed the pristine fabric's

https://doi.org/10.1038/s41467-026-68951-x

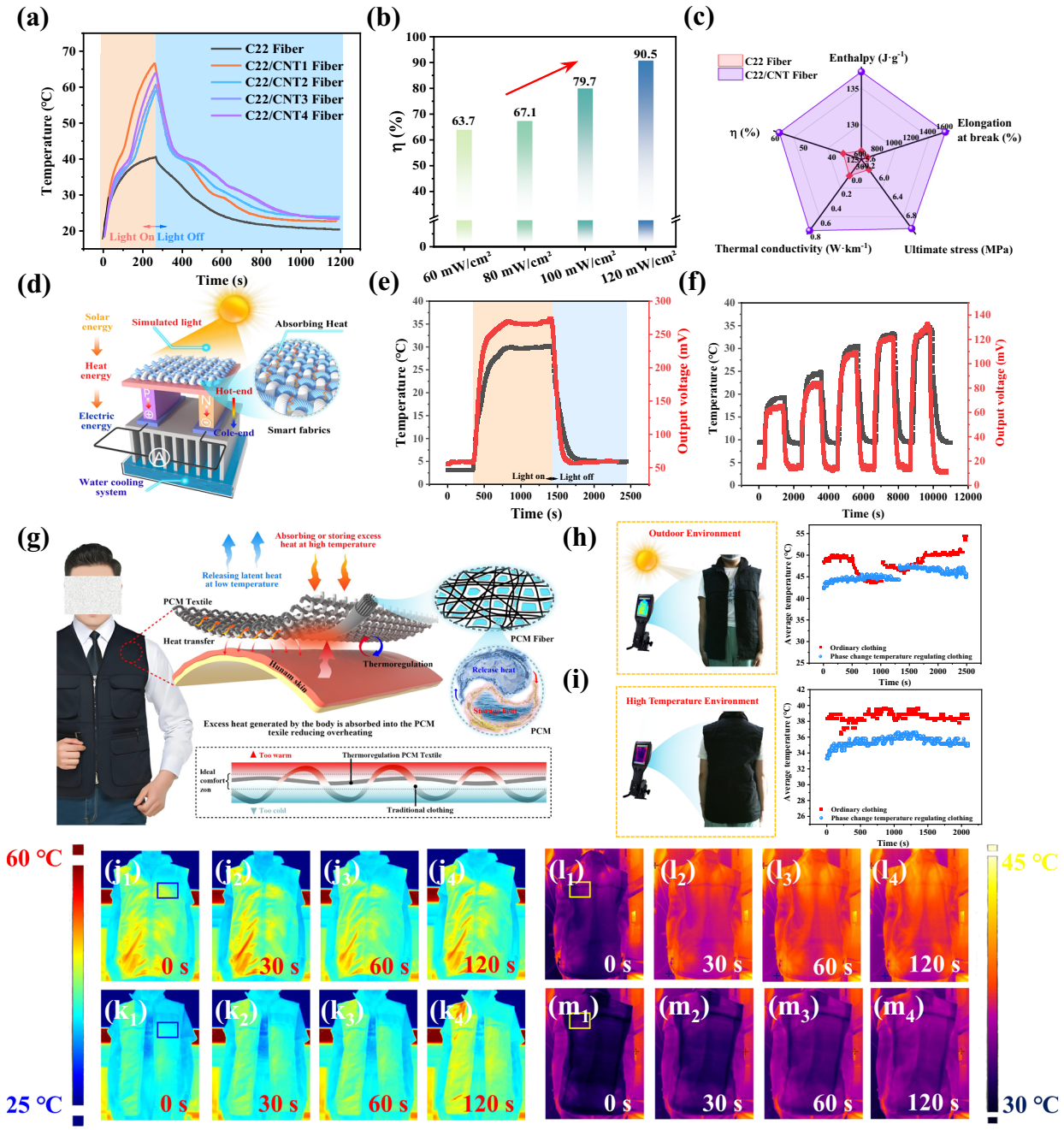

Fig. 6 | Photothermal and solar-to-electric energy conversion of CNT-PCTRFs for wearable thermal management. a Temperature evolution curves of CNT-PCTRFs (25 cm^2) by varying CNTs contents under 80 $mW{\cdot}cm^{-2}$ solar illumination. **b** η values of CNT-PCTRFs (25 cm^2) at varying light intensities. **c** Radar chart comparing C22 and C22/CNT fibers in latent heat, mechanical properties, thermal conductivity, and η values. **d** Experimental setup for solar thermoelectric conversion. Temperature and output voltage of CNT2-PCTRFs under 100 $mW{\cdot}cm^{-2}$ (**e**) and variable solar intensities (**f**). **g** Schematic of PCM garment thermal regulation using C22/CNT2 fibers. **h, i** Photos, and mean temperature comparison between ordinary vests and PCM-based garments under solar exposure (**h**), and at high-temperature work environments (**i**), with wearing-time evolution, respectively. $\mathbf{j_1}$–$\mathbf{m_4}$ Infrared thermography images of ordinary vest ($\mathbf{j_1}$–$\mathbf{j_4}$, $\mathbf{l_1}$–$\mathbf{l_4}$), and thermoregulation PCM garment ($\mathbf{k_1}$–$\mathbf{k_4}$, $\mathbf{m_1}$–$\mathbf{m_4}$) under solar exposure and high-temperature conditions at increasing wearing times, respectively.

efficiency of 34.5% by near double. This indicates that the CNT network can synergistically enhance solar energy conversion through photon trapping and anisotropic thermal conduction. Furthermore, the photothermal conversion efficiency of the fabric exhibited a direct correlation with the intensity of simulated solar irradiance intensity. As shown in Supplementary Fig. 47, when the simulated solar irradiation intensity was varied at 60, 80, 100, and 120 mW/cm^2, the η values for CNT2-PCTRF were observed to increase correspondingly: 63.7%, 67.1%, 79.7%, and 90.5%, respectively (see Fig. 6b). To assess the stability of the photothermal conversion capability, CNT2-PCTRF underwent 10 cycling tests (Supplementary Fig. 48). The consistent cyclic curves demonstrated the excellent stability of the material's photothermal performance. The optimized PCF with 0.1 wt.% CNT loading exhibited multifunctionality, including remarkable latent heat storage/release capacity ($\Delta H_m = 139.0\ J{\cdot}g^{-1}$, $\Delta H_m = 138.0\ J{\cdot}g^{-1}$), high mechanical properties ($\varepsilon = 1535\%$, $\sigma = 6.28$ MPa), and robust photothermal performance

(η = 58.9% at 80 mW·cm^{-2}). These attributes were comprehensively evaluated using a radar chart, providing a comprehensive overview of the performance of CNT-reinforced PCFs (Fig. 6c).

The photothermal properties of CNT2-PCTRF's were harnessed to assess its potential for solar-to-electric energy conversion, as illustrated in Fig. 6d. The experimental setup comprised three essential modules: a photothermal-electric conversion unit, a temperature monitoring apparatus, and a voltage acquisition system. Under simulated solar irradiation (1 Sun, AM 1.5), a solar thermoelectric generator (STEG) device was employed, utilizing CNT2-PCTRF as active heat source and stainless-steel radiators as the cold sink. The output voltage dynamics were continuously recorded during operation (Fig. 6e). At steady-state condition with a cold-side temperature maintained at approximately 5 °C, it was observed that the thermal energy discharged by CNT2-PCTRF at the hot junction of the thermoelectric module directly influenced the system's open-circuit voltage. This finding underscored the critical role of photothermal material efficiency in determining the overall performance of energy conversion. The integrated STEG system, incorporating CNT2-PCTRF as the heat source, achieved a notable output voltage of 280 mV at thermal equilibrium (Fig. 6e), demonstrating promising photo thermoelectric energy conversion capabilities. Upon the cessation of light exposure, the system experienced a rapid decline in output voltage due to the decrease in equilibrium temperature and subsequent release of stored thermal energy. Furthermore, increasing the intensity of incident solar radiation led to a proportional rise in CNT2-PCTRF's temperature, enabling substantial energy storage within the material. This phenomenon was reflected in enhanced voltage outputs across varying light intensities (from 60 mW·cm^{-2} to 140 mW·cm^{-2}), with corresponding voltage readings ranging from 60 mV to 140 mV (Fig. 6f). The system exhibited excellent stability, as evidenced by a minimal output variation of less than 2% over ten consecutive cycles (Supplementary Fig. 49) and an effective thermal boundary layer management mechanism. This result highlights the significant potential of CNT-PCTRF materials to store substantial amounts of thermal energy, which can be released to extend power supply duration. The demonstrated capability of CNT-PCTRFs in photo thermoelectric energy conversion further underscores their promising application in clean energy collection and augmentation of power supply systems.

The fabrication of CNT-PCTRFs and garments was successfully achieved using semi-automatic weaving machines and commercial sewing machines, respectively (Fig. 1f, g and Supplementary Fig. 11). The development of revolutionary manufacturing processes enabled scalable production of intelligent thermally regulated fabrics and garments, demonstrating significant potential for industrial applications. The seamless integration CNT-PCTRFs with commercial sewing technology opens up possibilities for their incorporation into diverse types of clothing and textiles, particularly for advanced wearable thermal management systems. Human metabolic heat generation involves the conversion of chemical energy from food intake into thermal energy, which is then dissipated to the surrounding environment through various mechanisms. Thermal comfort is conventionally achieved by adjusting the number of clothing layers or through the electrical consumption. The incorporation of carbon-based PCFs into textiles that exhibit high latent heat storage/release capacity (ΔH_m = 87.6 J·g^{-1}, ΔH_m = 85.0 J·g^{-1}) offers a promising solution for temperature regulation (Fig. 1e and Fig. 6g). Upon an increase in ambient temperature, the PCMs within the fibers undergo phase transition from solid to liquid, thereby absorbing and storing the heat energy. Conversely, during a decrease in temperature, the PCMs revert to their solid state, releasing the stored heat. This phase-changing mechanism enables the PTCs to function as self-regulating sensors and intelligent temperature controllers, automatically responding to ambient temperature changes while maintaining optimal body thermal comfort (Fig. 6g). Furthermore, the incorporation of CNTs into PCFs enhances their thermal conductivity of materials, imparting dominant functional properties such as efficient solar-thermal-electric energy conversion and excellent durability under continuous heating-cooling cycles.

We developed a wearable garment to evaluate the thermal regulation performance of the CNT-PCTRFs under real-world operational conditions, demonstrating their manufacturability and wearable integration for scalable thermal management applications. Field testing in Beijing, China, validated the ability of CNT-PCTRF to maintain human thermal comfort across various environments, including outdoor wearable validation and indoor thermal protection (Fig. 6h, i). To ensure the accuracy and uniformity of thermal measurements, temperature and thermal distribution were monitored using an infrared thermal imaging device (Fig. 6j_1–j_4, k_1–k_4, l_1–l_4, m_1–m_4). A volunteer participated in the study by wearing ordinary vests and specialized garments designed to regulate body temperature (PCM clothing), enabling an assessment of the practical wearability of phase-change textiles. This experiment took place on a sunny summer day at Peking University, where the participant wore the aforementioned vest and was exposed to direct sunlight for 30 minutes. Throughout this period, the thermal properties of the vests and volunteers were meticulously monitored (Fig. 6h, j_1–j_4, k_1–k_4). The data show that during peak solar irradiance, which occurred between 8:30 am and 10:30 am, the temperature of the thermoregulated PCM clothing (approximately 42 °C) was approximately 8 °C lower than that of the ordinary vest (approximately 50 °C). Infrared thermal imaging revealed a substantial temperature difference between the phase-change clothing and ordinary vest (Fig. 6j_1–j_4, k_1–k_4). Meanwhile, thermocouples attached beneath the vest between the body regions covered by different fabrics indicated a temperature difference of approximately 5 °C between the thermoregulated PCM clothing and the normal vest (Fig. 6h).

Conventional thermal protective clothing (TPC) typically incorporates multiple fabric layers, which enhances insulation by increasing padding thickness. However, this conventional approach can lead to bulkier clothing, reduced breathability, and impaired mobility and efficiency for users. To further evaluate the thermal protection and temperature regulation capabilities of the CNT-PCTRFs in high-temperature environments, volunteers wore an ordinary vest and thermoregulated PCM attire inside a high-temperature chamber where muffle furnaces were operated at 1000 °C. Infrared thermography was used to observe the heat distribution and temperature changes between the garment and human body. The experiment demonstrated that conventional clothes rapidly elevated the temperature to the same level as the wearer in a high-temperature environment, and with volunteers perceiving significant heat transfer from their surroundings (Fig. 6l_1–l_4). In contrast, PCM clothing release heat to the environment before reaching their phase-change temperature, thereby help maintain the body at a comfortable temperature (Fig. 6i and Fig. 6m_1–m_4). Thermocouple readings revealed a temperature difference of approximately 4 °C between the thermoregulated PCM clothing and the ordinary vest. These results indicate that CNT-PCTRFs can effectively regulate and control heat while maintaining breathability and providing a comfortable wear experience. The findings underscore the importance of thermal protective textiles in safeguarding individuals from extreme high-temperature conditions.

The integration of CNT-PCTRFs through weaving, cutting, and commercial enables their use in a wide range of products tailored for various applications, such as clothing, tents, car covers, curtains, and awnings, and other similar items. Wearable and smart textiles incorporating PCMs provide adaptive temperature control and thermal management, ensuring personal thermal comfort without requiring external power or input. When applied for personal physical comfort, this passive technology delivers thermal comfort as the wearer's body temperature rises. Furthermore, this passive system proves particularly advantageous in extreme environmental conditions and holds potential for addressing certain medical needs.

Discussion

In summary, we introduce a scalable and cost-effective physical-crosslinking strategy for fabricating PCFs with high thermal storage density and long-term stability. Our integrated experimental and molecular dynamics studies elucidate three synergistic strategies to optimize PCFs performance: 3D-IPNs confinement engineering, CNT-induced structural modulation, and a scalable manufacturing paradigm. For the large-scale production, bi-component melt spinning and multi-stage confinement strategies provide practical and cost-efficient pathway for creating elastic support frameworks with high-molecular-weight polymers. The strategic incorporation of ultra-low CNT loading (0.1 wt.%) into PCFs enables three-dimensional reinforcement, achieving noticeable multifunctionality: enhanced latent heat amplification ($\Delta H_m = 139.0\ J{\cdot}g^{-1}$, $\Delta H_c = 138.0\ J{\cdot}g^{-1}$), accelerated thermal transport ($0.31\ W{\cdot}m^{-1}K^{-1}$), toughness enhancement ($\varepsilon = 1583\%$, $\sigma = 6.83$ MPa), and thermal reliability. Notably, the addition of 0.1 wt% CNTs increases enthalpy by 10 %, enhances thermal conductivity by 138.5%, and boosts elongation at break by 130.0%. MD simulations reveal two key mechanisms driving these improvements: CNT-induced crystallization and gradient-interface-engineering-induced fiber orientation. Furthermore, the composite PCM-based fabric fabricated via warp-weft weaving exhibited excellent photothermal and photo thermoelectric conversion properties. Using cutting and conventional sewing techniques, we fabricated PCM-based thermoregulatory clothing that outperforms traditional polyester fabrics in thermal regulation, maintaining stable thermal conditions under dynamic environmental temperatures. These advancements enable the scalable production of functional PCM-based textiles for high-power-density personal thermal management and protection. They hold transformative potential for wearable systems in extreme-environment applications and medical thermotherapy applications.

Methods

Materials

The base PCM, n-docosane (C22), was supplied by the Shanghai Mackin Biochemical Technology Co. Ltd. (China) and had a melting temperature of 42 °C. Styrene Ethylene Butylene Styrene (SEBS) (Mw = 16.1 w) and high-density polyethylene (HDPE) (Mw = 20 w) are preferred polymer-supporting materials. SEBS (Mw = 16.1 w) is a linear triblock copolymer with polystyrene as the end segment and an ethylene-butene copolymer obtained by the hydrogenation of polybutadiene as the intermediate elastic block. HDPE (Mw = 20 w) exhibits significant thermoplasticity. These materials were purchased from Kunshan Huayi Plastic Co. Ltd. (China) and Sinopec Yangzi Petrochemical Co. Ltd. (China). Carbon nanotubes (CNTs) with a diameter of 20 nm and a length of 10–30 μm were provided by Heowns Biochem Technologies Co., Ltd. as the additive agent.

Preparation of C22/CNT@SEBS-HDPE composite

Prior to use, n-docosane was heated to melt into a liquid state at 80 °C, and different dosages of CNTs were uniformly dispersed in n-docosane using ultrasonic cavitation at room temperature for 45 min. Subsequently, CNTs with different mass fractions (0, 0.05, 0.1, 0.5, and 1 wt. %) were dissolved in n-docosane. SEBS and HDPE were dissolved in n-docosane and CNTs composites to yield gel blocks. The gel blocks were subsequently introduced into an internal mixer (HTK-55, Guangzhou Hartek Technology Co., Ltd., China) and subjected to high-temperature mixing (175 °C) for 45 min. This process was performed to obtain a uniform C22/CNT@SEBS-HDPE composite material. Subsequently, the composite was cooled and added to the crusher, resulting in a uniform phase-change masterbatch with a size of 1 – 2 mm.

Preparation of C22/CNT fibers

Prior to the initiation of the spinning process, it was necessary to increase the temperature of the three stages of the twin-screw equipment to 120 °C, 140 °C, and 170 °C. Subsequently, a phase-change masterbatch was introduced into the feed inlet of the heat exchanger. Following a stepwise heating process, the polymer-based PCM was subjected to further mixing, resulting in the complete intertwining of the long molecular chains, thereby providing a restricted skeleton for n-docosane, which resulted in the formation of primary fibers. The extrusion rate was set to 1.5 m/min, whereas the curling and winding rates were 50 m/min. After three stretching cycles, the primary fibers underwent multiple stretching orientations, with C22 being confined further during this process. This resulted in carbon-based PCFs with uniform fiber diameters that were rolled into a roll. The production process can be summarized as follows: a continuous flow of viscous molten thermoplastic polymer is extruded through a spinneret. Subsequently, the polymer fibers are subjected to rapid cooling and solidification using cold air or a gas. Subsequently, the solidified fibers are collected after multiple stretching orientations and are further processed to yield the final product.

Preparation of CNT-PCTRFs

The employment of C22/CNT fibers as warp yarns and polyester yarns as weft yarns enabled the fabrication of CNT-PCTRFs using a semi-automatic loom. The preparation of thermoregulated PCM clothing entailed the design, cutting, and commercial sewing of four pieces of CNT-PCTRFs using a commercial sewing machine.

Characterization

The microstructure of the fibers coated with Au nanoparticles was characterized using a scanning electron microscope (SEM, HITACHI Regulu 8200, Japan) at an acceleration voltage of 5–10 kV. The fibers were sputtered with Au nanoparticles at an electric current 40 mA for 100 s. The microstructure of carbon nanotubes (CNTs) was examined using transmission electron microscopy (TEM, HITACHI H-7650, Japan) by depositing them onto a holey carbon support film. The fibers were prepared as ultrathin sections and subsequently analyzed using a field-emission high-resolution transmission electron microscope (JEM-2100F, Japan) at an acceleration voltage of 200 kV. Wide-angle X-ray diffraction (XRD, Rigaku SmartLab, Nexsa, Czech Republic) was used to investigate the crystalline structure at a scanning rate of 0.05 s over a 2 θ range of 5–60°. In-situ XRD measurements were conducted to determine the relationship between the crystallization peaks and temperature changes. In situ tensile tests were performed on the fiber samples using a small-angle X-ray scattering instrument (SAXS, Xenocs, Xeuss 3.0 HR, France). Differential scanning calorimetry (DSC) curves were recorded using a differential scanning calorimeter (DSC, PE, LN2-DSC8500, USA) at a heating/cooling rate of 5 °C min^{-1} under a nitrogen atmosphere between 0 and 80 °C. The cyclic durability of the samples was assessed using DSC within the same temperature range at a rate of 10 °C min^{-1} for 125 cycles under nitrogen protection. Thermal gravimetric analysis (TGA) was conducted using a thermogravimetric analyzer (TA, SDT Q600, USA) at a heating rate of 15 °C min^{-1} from 40 to 800 °C in a nitrogen atmosphere. Thermal conductivity was measured using an integrated physical property measurement system (PPMS, Quantum Design PPMS-9, USA) in a vacuum environment, and the results were averaged from multiple measurements. A polarizing optical microscope (POM) was employed for the real-time observation of alterations in the crystal structure during the heating and cooling cycles of the samples within the temperature range of 20–50 °C. The mechanical properties of the fibers were assessed using a single-column mechanical testing system (Instron 5843, USA) in the tensile mode at a tensile rate of 50 mm min^{-1}. The light-to-thermal conversion experiments were conducted under simulated sunlight illumination provided by a CEL-S500 xenon lamp (Zhongjiao Jinyuan Company, China) with an AM 1.5 filter. The intensity of simulated solar sunlight illumination was calibrated using an optical power meter (CEL-FZ-A). The relationship between the surface temperature of the samples and

the illumination time was measured and recorded using a high-precision digital thermometer (DP700, RKC Japan) connected to a thermocouple (ST-50). Thermal images of the heat distribution on the surface of the measured object were captured by using an infrared thermal imager.

Fore field of molecular dynamics (MD) simulation

All MD simulations for crystallization process and stretching process were performed using LAMMPS. Trajectory visualization and analysis were facilitated by using VMD software. The simulations employed the all-atom OPLS-AA force field. More detailed information is available in the Supplementary Information.

Data availability

The data generated and analyzed during this study are provided in the main text and the Supplementary Information. All data are also available from the corresponding author upon request. Source data are available at https://doi.org/10.6084/m9.figshare.31025938.

References

1. Creutzig, F. Fuel crisis: slash demand in three sectors to protect economies and climate. *Nature* **606**, 460–462 (2022).
2. Zeng, S. et al. Hierarchical-morphology metafabric for scalable passive daytime radiative cooling. *Science* **373**, 692–696 (2021).
3. Ma, W. et al. Smart fibers for energy conversion and storage. *Chem. Soc. Rev.* **50**, 7009–7061 (2021).
4. Peng, Y. & Cui, Y. Advanced Textiles for Personal Thermal Management and Energy. *Joule* **4**, 724–742 (2020).
5. Zhang, X. A. et al. Dynamic gating of infrared radiation in a textile. *Science* **363**, 619–623 (2019).
6. Tebyetekerwa, M. et al. Critical insight: challenges and requirements of fibre electrodes for wearable electrochemical energy storage. *Energy Environ. Sci.* **12**, 2148–2160 (2019).
7. Wang, G. et al. Phase Change Thermal Storage Materials for Interdisciplinary Applications. *Chem. Rev.* **123**, 6953–7024 (2023).
8. Chen, X. et al. Optimization strategies of composite phase change materials for thermal energy storage, transfer, conversion and utilization. *Energy Environ. Sci.* **13**, 4498–4535 (2020).
9. Aftab, W. et al. Phase change material-integrated latent heat storage systems for sustainable energy solutions. *Energy Environ. Sci.* **14**, 4268–4291 (2021).
10. Gulfam, R., Zhang, P. & Meng, Z. Advanced thermal systems driven by paraffin-based phase change materials – A review. *Appl Energy* **238**, 582–611 (2019).
11. Liu, H. et al. Intrinsically Flexible Phase Change Fibers for Intelligent Thermal Regulation. *Angew. Chem. Int Ed. Engl.* **63**, e202408857 (2024).
12. Zhu, Z. et al. Highly Integrated Phase Change and Radiative Cooling Fiber Membrane for Adaptive Personal Thermal Regulation. *Adv. Funct. Mater.* **35**, 2416111 (2024).
13. Wang, S., Du, R. & Li, T. Progress and perspective on thermal conductivity enhancement of phase change materials. *Sci. Bull.* **69**, 3176–3179 (2024).
14. Luo, J. et al. Fabricating strong and tough aramid fibers by small addition of carbon nanotubes. *Nat. Commun.* **14**, 3019 (2023).
15. Liu, Y. et al. Muscle-Inspired Formable Wood-Based Phase Change Materials. *Adv. Mater.* **36**, e2406915 (2024).
16. Li, C. et al. Tunable superconductivity in electron- and hole-doped Bernal bilayer graphene. *Nature* **631**, 300–306 (2024).
17. Geng, X. et al. Muscle-inspired super-flexible phase change materials with programmable deformation for photothermal actuation. *Adv. Funct. Mater.* **35**, 2418848 (2024).
18. Yan, D. et al. Carbon Nanotube-Directed 7 GPa Heterocyclic Aramid Fiber and Its Application in Artificial Muscles. *Adv. Mater.* **36**, 2306129 (2023).
19. Wu, Y. et al. Recyclable solid-solid phase change materials with superior latent heat via reversible anhydride-alcohol crosslinking for efficient thermal storage. *Adv. Mater.* **36**, e2311717 (2024).
20. Shi, J., Qin, M., Aftab, W. & Zou, R. Flexible phase change materials for thermal energy storage. *Energy Storage Mater.* **41**, 321–342 (2021).
21. Jing, Y. G. et al. Ultraflexible, cost-effective and scalable polymer-based phase change composites via chemical cross-linking for wearable thermal management. *Nat. Commun.* **14**, 8060 (2023).
22. Peng, Y. & Cui, Y. Thermal management with innovative fibers and textiles: manipulating heat transport, storage and conversion. *Natl. Sci. Rev.* **11**, nwae295 (2024).
23. Chen, X., Xu, J., Li, Y., Gao, Y. & Wang, G. Integrating multiple energy storage in 1D–2D bridged array carbon-based phase change materials. *SusMat* **3**, 510–521 (2023).
24. Freeman, T. B. et al. Advanced materials and additive manufacturing for phase change thermal energy storage and management: a review. *Adv. Energy Mater.* **13**, 2204208 (2023).
25. Yazdani McCord, M. R., Zimmerman, J. B. & Rojas, O. J. Harnessing multifunctional electrospun nanofibers containing phase change materials for energy-efficient thermal management: A review on recent trends. *Nano Energy* **131**, 110212 (2024).
26. Wu, Y. et al. Preparation and melt-spun applications of PA6-based Poly(Amide-Ether) copolymers phase change fibers with passive temperature management. *Chem. Eng. J.* **500**, 157359 (2024).
27. Gu, B. et al. A novel method for increasing phase-change microcapsules in nanofiber textile through electrospinning. *Adv. Funct. Mater.* **35**, 2412089 (2024).
28. Jordan, J. L. et al. Elastic properties of polyethylene from high pressure sound speed measurements. *Polymer* **212**, 123164 (2021).
29. Porter D. A. & Easterling K. E. *Phase Transformations in Metals and Alloys (CRC Press, 2009)*.
30. Valentini, L., Biagiotti, J., Kenny, J. M. & Santucci, S. Effects of single-walled carbon nanotubes on the crystallization behavior of polypropylene. *J. Appl. Polym. Sci.* **87**, 708–713 (2002).
31. Xia, W. et al. Nano-hybridized form-stable ester@F-SiO_2 phase change materials for melt-spun PA6 fibers engineered towards smart thermal management fabrics. *Chem. Eng. J.* **403**, 126369 (2021).
32. Wang, W. et al. Continuous fibers featuring high phase change enthalpy fabricated by melt spinning for thermal management. *J. Energy Storage* **100**, 113690 (2024).
33. Zhang, G., Xu, S., Du, M., Liu, G. & Zhou, L. Temperature regulating fibers of high latent heat and strength: Mass production, characterization and applications. *J. Energy Storage* **42**, 103030 (2021).
34. Chen, Z. et al. Controllable large-scale processing of temperature regulating sheath-core fibers with high-enthalpy for thermal management. *Nano Mater. Sci.* **6**, 337–344 (2024).
35. Lan, T. Y. et al. A rapid thermal absorption rate and high latent heat enthalpy phase change fiber derived from bio-based low melting point copolyesters. *Polymers* **14**, 3298 (2022).
36. Liu, Z. et al. Fabrication and performance of phase change thermoregulated fiber from bicomponent melt spinning. *Polymers* **14**, 1895 (2022).
37. Zhang, R., Feng, P. & Yang, C. Preparation and analysis of sheath-core intelligent thermo-regulating fiber. *Polymers* **14**, 1665 (2022).
38. Zhai, M. et al. Effective antibacterial and phase change PEG/Cu_2O@A-HNTs composites for melt-spun difunctional PA6 fiber. *Prog. Nat. Sci: Mater. Int* **32**, 776–785 (2022).
39. Xiao, J. et al. Large-scale production of continuous sheath-core composite phase change fibers for personal thermal management in cold alpine environments by coaxial wet spinning technology. *ACS Appl Energy Mater.* **7**, 4494–4503 (2024).
40. Yang, K. et al. Smart and robust phase change cellulose fibers from coaxial wet-spinning of cellulose nanofibril-reinforced paraffin

capsules with excellent thermal management. *Carbohydr. Polym.* **346**, 122649 (2024).
41. Cao, H., Xu, Z., Zhang, T. & Zhao, Y. Highly stretchable phase change fibers from coaxial wet spinning of nonaqueous emulsions for temperature regulation. *Chem. Eng. J.* **478**, 147389 (2023).
42. Zhang, J. et al. Weavable coaxial phase change fibers concentrating thermal energy storage, photothermal conversion and thermochromic responsiveness toward smart thermoregulatory textiles. *Chem. Eng. J.* **483**, 149281 (2024).
43. Niu, Z., Qi, S., Shuaib, S. S. A. & Yuan, W. Flexible, stimuli-responsive and self-cleaning phase change fiber for thermal energy storage and smart textiles. *Compos Part B: Eng.* **228**, 109431 (2022).
44. Geng, J. et al. Photo-thermal and temperature-regulated sodium alginate-g-mPEG/carbon nanotube hybrid fibers with improved tensile strength. *Int J. Biol. Macromol.* **282**, 137109 (2024).
45. Hu, L. et al. A hierarchical core-sheath structure composite fiber of PW/TPU towards elastic smart thermal management fabrics. *J. Energy Storage* **77**, 109802 (2024).
46. Xu, F., Zhang, T., Xu, Z. & Zhao, Y. Solid-solid phase change fibers with enhanced energy storage density for temperature management. *J. Energy Storage* **79**, 110190 (2024).
47. Li, W., Xu, L., Wang, X., Zhu, R. & Yan, Y. Phase Change Energy Storage Elastic Fiber: A Simple Route to Personal Thermal Management. *Polymers* **14**, 53 (2021).
48. Niu, Z., Qi, S., Shuaib, S. S. A., Züttel, A. & Yuan, W. Flexible core-sheath thermochromic phase change fibers for temperature management and electrical/solar energy harvesting. *Compos Sci. Technol.* **226**, 109538 (2022).
49. Xu, C. et al. 3D cotton-like phase change fibers via electrospinning for thermal management of textile. *J. Energy Storage* **84**, 110991 (2024).
50. Wu, J. et al. A trimode thermoregulatory flexible fibrous membrane designed with hierarchical core-sheath fiber structure for wearable personal thermal management. *ACS Nano* **16**, 12801–12812 (2022).
51. Li, X. et al. Wearable Janus-type film with integrated all-season active/passive thermal management, thermal camouflage, and ultra-high electromagnetic shielding efficiency tunable by origami process. *Adv. Funct. Mater.* **33**, 2212776 (2023).
52. Wu, J. et al. Highly integrated, breathable, metalized phase change fibrous membranes based on hierarchical coaxial fiber structure for multimodal personal thermal management. *Chem. Eng. J.* **465**, 142835 (2023).
53. Wang, S. et al. Reversibly thermochromic and high strength core-shell nanofibers fabricated by melt coaxial electrospinning. *J. Appl Polym. Sci.* **138**, 50465 (2021).
54. Wu, F. et al. Multifunctional flexible composite membrane based on nanocellulose-modified expanded graphite/electrostatically spun fiber network structure for solar thermal energy conversion. *Energy Rep.* **11**, 4564–4571 (2024).
55. Qin, Z. et al. Nanofibrous membranes with hydrophobic and thermoregulatory functions fabricated by coaxial electrospinning. *J. Appl Polym. Sci.* **140**, e54677 (2023).
56. Baniasadi, H., Madani, M., Seppälä, J., Zimmerman, J. B. & Yazdani, M. R. Form-stable phase change electrospun nanofibers mat with thermal regulation and biomedical multi-functionalities. *J. Energy Storage* **68**, 107660 (2023).
57. Jing, H. et al. Flexible electrospun porous carbon nanofiber@PEG phase change nanofibrous membrane for advanced solar-/electro-thermal energy conversion and storage. *J. Energy Storage* **104**, 114608 (2024).
58. Wang, J., Xu, J. & He, Y. Novel smart textile with ultraviolet shielding and thermo-regulation fabricated via electrospinning. *J. Energy Storage* **42**, 103094 (2021).
59. Wang, S. et al. Multifunctional nanofiber membrane with anti-ultraviolet and thermal regulation fabricated by coaxial electrospinning. *J. Ind. Eng. Chem.* **108**, 449–455 (2022).
60. Qiao, J. et al. Flexible highly thermally conductive pcm film prepared by centrifugal electrospinning for wearable thermal management. *Materials* **17**, 4963 (2024).
61. Lin, Y. et al. Flexible, highly thermally conductive and electrically insulating phase change materials for advanced thermal management of 5G base stations and thermoelectric generators. *Nano-Micro Lett.* **15**, 31 (2023).
62. Wang, S. et al. Preparation of core-sheath nanofibers with high latent heat by thermal cross-linking and coaxial electrospinning. *Polymer* **228**, 123958 (2021).
63. Fredi, G., Kianfar, P., Dalle Vacche, S., Pegoretti, A. & Vitale, A. Electrospun shape-stabilized phase change materials based on photo-crosslinked polyethylene oxide. *Polymers* **13**, 2979 (2021).
64. Ma, Y., Shen, J., Li, T., Sheng, X. & Chen, Y. A "net-ball" structure fiber membrane with electro-/photo-thermal heating and phase change synchronous temperature regulation capacity via electrospinning. *Sol. Energy Mater. Sol. Cells* **276**, 113078 (2024).
65. Pan, C. et al. A multifunctional flexible composite film with excellent insulation flame retardancy, thermal management and solar-thermal conversion properties based on CNF-modified mica/electrospun fibrous networks structure. *Sol. Energy Mater. Sol. Cells* **261**, 112530 (2023).

Acknowledgements

The authors gratefully acknowledge the financial support for this research from the National Key Research and Development Program of China (grant no. 2020YFA0210701), the China National Petroleum Corporation-Peking University Strategic Cooperation Project of Functional Research, and the National Natural Science Foundation of China (grant no. 52475001). We would like to express our gratitude to the Materials Processing and Analysis Center, Peking University, for their assistance with SEM and XRD characterization. We sincerely acknowledge the Analytical Instrumentation Center, Peking University, for their professional assistance with HRTEM characterization. We are also deeply grateful to Professor Qian Wang from the School of Materials Science and Engineering at Peking University for his valuable guidance and advice regarding the MD simulations in this work. All authors participated in a thorough discussion of the results and analysis of the data, and approved the submission of the final version.

Author contributions

X.G. was responsible for the study conception, experimental design, theoretical calculations, data analysis, and writing the initial manuscript. Z.W. collaborated on performing the experiments and data analysis. F.X. assisted with structural characterization. L.L. contributed to the preparation and weaving of fabric-based materials. Z.Z., Y.J., M.Q., J.S., and S.G. contributed to data collection and validation. Y.W. provided technical support. Q.W. and R.Z. supervised the project, coordinated the collaboration, and critically revised the manuscript. All authors discussed the results and approved the final manuscript.

Competing interests

The authors declare no competing interests.

Informed consent

Written informed consent was obtained from all volunteers following a detailed explanation of the study and a confirmed understanding of its procedures.

Additional information

Supplementary information The online version contains supplementary material available at https://doi.org/10.1038/s41467-026-68951-x.

Correspondence and requests for materials should be addressed to Qining Wang or Ruqiang Zou.

Peer review information *Nature Communications* thanks Ronghui Wu and the other, anonymous, reviewer(s) for their contribution to the peer review of this work. A peer review file is available.